

# Synthesis and Electrochemical Properties of $\text{Fe}_x\text{NbS}_2/\text{C}$ Composites as an Anode Material for Li Secondary Batteries

Yunjung Kim and Jae-Hun Kim<sup>†</sup>

*School of Materials Science and Engineering, Kookmin University, Seoul 02707, Republic of Korea*

(Received August 04, 2022; Revised August 04, 2022; Accepted August 17, 2022)

Transition metal sulfide materials have emerged as a new anode material for Li secondary batteries owing to their high capacity and rate capability facilitated by fast Li-ion transport through the layered structure. Among these materials, niobium disulfide ( $\text{NbS}_2$ ) has attracted much attention with its high electrical conductivity and high theoretical capacity ( $683 \text{ mAh g}^{-1}$ ). In this study, we propose a facile synthesis of  $\text{Fe}_x\text{NbS}_2/\text{C}$  composite via simple ball milling and heat treatment. The starting materials of FeS and Nb were reacted in the first milling step and transformed into an Fe-Nb-S composite. In the second milling step, activated carbon was incorporated and the sulfide was crystallized into  $\text{Fe}_x\text{NbS}_2$  by heat treatment. The prepared materials were characterized by X-ray diffraction, electron spectroscopies, and X-ray photoelectron spectroscopy. The electrochemical test results reveal that the synthesized  $\text{Fe}_x\text{NbS}_2/\text{C}$  composite electrode demonstrates a high reversible capacity of more than  $600 \text{ mAh g}^{-1}$ , stable cycling stability, and excellent rate performance for Li-ion battery anodes.

**Keywords:** *Transition metal dichalcogenide, Niobium sulfide, Composite, Li battery, Electrochemical properties*

## 1. Introduction

For several decades, global efforts to move away from fossil fuels have continued. Amid these changes, various energy storage systems have emerged, such as batteries, supercapacitors, and fuel cells. Among these energy storage systems, Li-ion batteries have been recognized for their high energy density and cycle life; therefore, they have been widely used in portable electronic devices and electric vehicles [1,2]. However, the energy densities and rate properties of these batteries cannot meet the current market demands; accordingly, various alternative electrode materials have been developed [3-5]. Graphite-based materials are currently used as negative electrode materials owing to their moderate capacity, good cycle stability, and low cost [6-8]. Because graphite uses intercalation chemistry for Li storage (theoretical capacity:  $372 \text{ mAh}^{-1}$ ), it has limitations in terms of capacity and rate capability. To overcome these limitations, there has been active research on alternative anode materials, such as Li-alloy-based materials and transition metal oxides/sulfides

that store Li-ions via alloying and conversion mechanisms [9-12].

Among the alternative materials, transition metal dichalcogenides (TMDs) have received considerable attention due to their unique chemical and physical characteristics. TMDs have a layered structure with a general formula of  $\text{MX}_2$  (M: transition metal, X: chalcogen atom) where M is sandwiched between the two X atoms. The layered X-M-X structure is stacked together by weak van der Waals forces [13]. This layered structure facilitates the rapid transport of ions and electrons in Li storage electrodes [13,14]. For use as high-rate electrode materials, the TMD materials usually go through a process in which each layer is separated after synthesis, such as wet-chemical exfoliation, mechanical cleavage exfoliation, and chemical and physical vapor deposition [15,16]. Among the TMD materials,  $\text{NbS}_2$  is considered an attractive candidate because of its high theoretical capacity ( $683 \text{ mAh}^{-1}$ ) based on the conversion reaction mechanism [17,18].  $\text{NbS}_2$  is mainly produced through a high-temperature solid-state synthesis between  $700 \text{ }^\circ\text{C}$  and  $1050 \text{ }^\circ\text{C}$  and then subjected to the wet-chemical exfoliation process, which can be inefficient in terms of cost and production yield [19-22].

<sup>†</sup>Corresponding author: [jaehunkim@kookmin.ac.kr](mailto:jaehunkim@kookmin.ac.kr)  
Yunjung Kim: Researcher, Jae-Hun Kim: Professor

In this study, we propose a facile synthesis of Fe-substituted  $\text{NbS}_2$  material via a high-energy mechanical milling (HEMM) process as alternative anode materials for Li-ion batteries. The starting materials were FeS and Nb powders. During the first HEMM step, Fe in FeS was partially replaced by Nb to produce  $\text{Fe}_x\text{Nb}_y\text{S}$ . In the second milling step, carbon was incorporated to buffer the volume change in the active material and to increase electronic conductivity. Then, the heat treatment and etching process led to the formation of the  $\text{Fe}_x\text{NbS}_2/\text{C}$  composite ( $x \sim 0.5$ ), where Fe atoms are intercalated between the  $\text{NbS}_2$  layers. The electrochemical test results demonstrate that the synthesized  $\text{Fe}_x\text{NbS}_2/\text{C}$  composite electrodes exhibit a high capacity of approximately  $600 \text{ mAh g}^{-1}$  at 0.1 C, which is much higher than that of graphite anodes. The capacity of approximately  $310 \text{ mAh g}^{-1}$  was obtained even at a high rate of 5 C.

## 2. Experimental

### 2.1 Material preparation

The composite materials were prepared by a two-step milling process. First, Nb (0.7 g, Alfa Aesar, 99.8%) and FeS (1.3 g, Sigma Aldrich, 99.9%) powders were added to a steel vial, and steel balls were put into the vial at a weight ratio of 1:20. The milling process was performed under an Ar atmosphere at 800 rpm for 12 h. Then, the resulting composite was milled with activated carbon (Super P) as a second step under the same conditions. To obtain the  $\text{Fe}_x\text{NbS}_2$  phase, the as-prepared composite was heated in a vertical furnace at  $900^\circ\text{C}$  for 2 h under an Ar atmosphere. Then, to remove the residual Fe in the composite, chemical etching was performed with an ethanol solution containing 5% nitric acid ( $\text{HNO}_3$ ) for a few minutes. Finally, the samples were washed several times with ethanol and dried overnight in a vacuum oven at  $60^\circ\text{C}$ .

### 2.2 Material characterization

To ascertain the crystal structure of the composite samples, X-ray diffraction (XRD, Rigaku Ultima IV) was conducted. Raman spectroscopy (Renishaw) and X-ray photoelectron spectroscopy (XPS, Thermo Scientific K-alpha) were performed to identify the chemical bonding states of the material. Field-emission scanning electron

microscopy (FE-SEM, JEOL JSM 7401F) with energy dispersive spectroscopy (EDS) and transmission electron microscopy (TEM, FEI Talos) were employed to examine the morphology and structural characteristics of the synthesized composites.

### 2.3 Electrochemical measurements

To characterize the electrochemical properties of the synthesized material, coin-type half cells (CR2032) were employed. The working electrodes were prepared by coating slurries consisting of an active material (70 wt%), a conductive agent (Super P, 15 wt%), and a binder (polyvinylidene fluoride, 15 wt%) on copper foil. Then, the electrodes were dried in a vacuum oven at  $120^\circ\text{C}$  for 12 h. Li foils were used as counter and reference electrodes. The electrolyte was 1.0 M  $\text{LiPF}_6$  in ethylene carbonate and dimethyl carbonate (3:7 by volume ratio) with a 10 wt% fluoroethylene carbonate solution, and a porous polyethylene separator was used. The coin cells were assembled in an Ar-filled glove box. The galvanostatic discharge-charge tests were carried out using a battery tester (Basytec CTS-Lab) in the potential window of 0.01–3.0 V (vs.  $\text{Li}^+/\text{Li}$ ) at  $25^\circ\text{C}$ . The rate capability was measured under various rates (0.1–5C, 1C =  $600 \text{ mAh g}^{-1}$ ) under the same conditions.

## 3. Results and Discussion

Fig. 1 shows the schematic illustration of the synthesis process of the  $\text{Fe}_x\text{NbS}_2/\text{C}$  composite. In the first step, several interatomic bonds in FeS were broken, and the Nb atoms substituted the vacant positions. The second HEMM step with activated carbon powders (Super P) and heat treatment resulted in the formation of the  $\text{Fe}/\text{Fe}_x\text{NbS}_2/\text{C}$  composite, where  $\text{Fe}_x\text{NbS}_2$  and Fe particles were embedded in the composite. Finally, via the wet etching process with the  $\text{HNO}_3$  solution, the Fe particles were completely removed and the  $\text{Fe}_x\text{NbS}_2/\text{C}$  composite was successfully fabricated.

To examine the crystal structure and internal chemical bonds, X-ray diffraction and Raman spectroscopy were employed. Fig. 2a presents the XRD patterns of the  $\text{Fe}_x\text{NbS}_2/\text{C}$  composite with those of the starting materials (FeS and Nb) and the reference pattern. The peaks at approximately  $14.4^\circ$ ,  $28.9^\circ$ ,  $30.9^\circ$ ,  $31.8^\circ$ ,  $34.3^\circ$ ,  $38.0^\circ$ ,

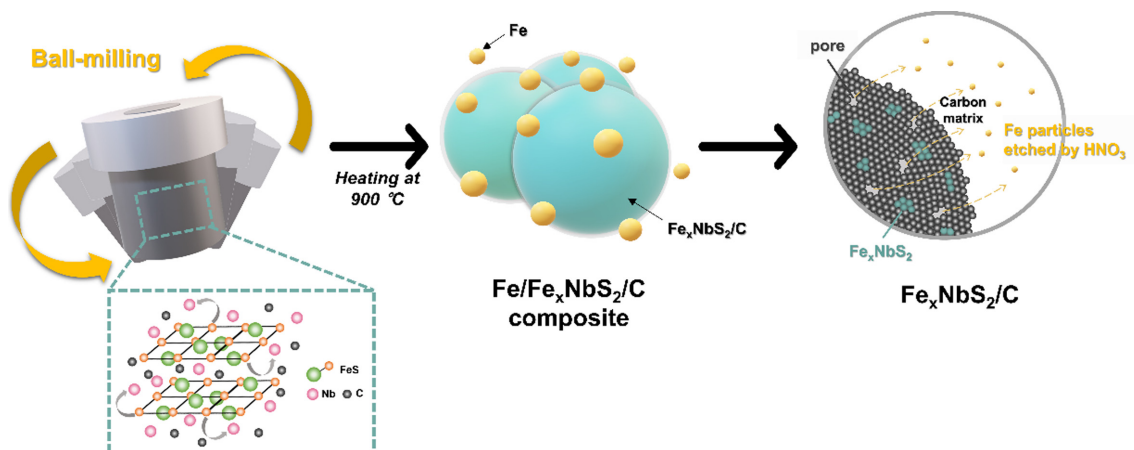


Fig. 1. Schematic illustration for the synthesis of the  $\text{Fe}_x\text{NbS}_2/\text{C}$  composite

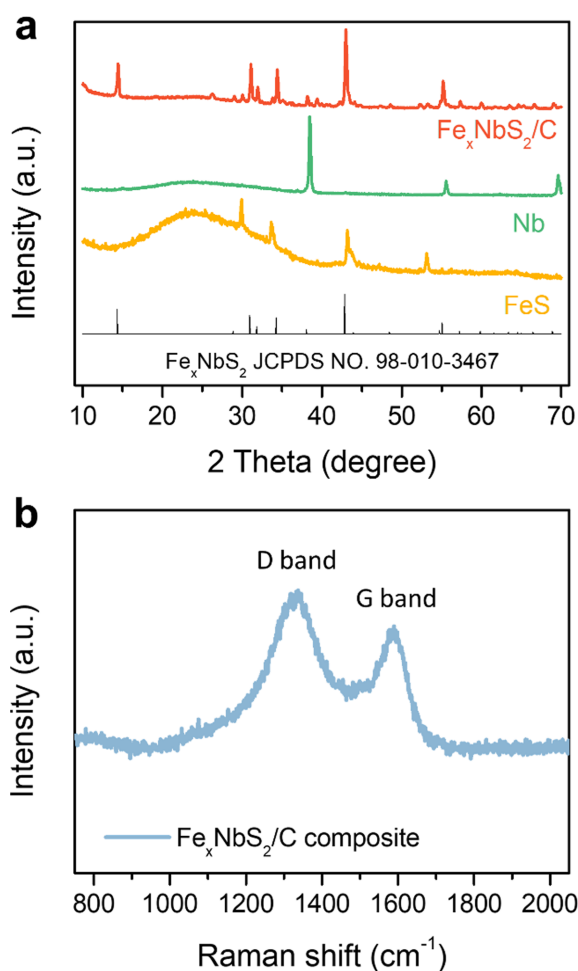


Fig. 2. (a) XRD patterns of the synthesized  $\text{Fe}_x\text{NbS}_2/\text{C}$  composite with reference patterns and (b) Raman spectrum of the  $\text{Fe}_x\text{NbS}_2/\text{C}$  composite

42.8°, 43.9°, 48.5°, 54.7°, and 55.0° can be indexed to the (002), (004), (010), (011), (012), (013), (014), (006), (015), (016), and (110) reflection planes of the  $\text{Fe}_{0.49}\text{NbS}_2$

phase (JCPDS 98-010-3467, hexagonal), respectively [23]. The results indicate that the  $\text{Fe}_x\text{NbS}_2$  phase ( $x \sim 0.5$ ) was successfully prepared through the synthesis procedures. Fig. 2b shows the Raman spectrum of the  $\text{Fe}_x\text{NbS}_2/\text{C}$  composite. The bands at approximately  $1350\text{ cm}^{-1}$  and  $1600\text{ cm}^{-1}$  can be attributed to the D and G bands of carbon, which confirm the incorporation of carbon into the composite.

Fig. 3 presents the XPS wide scan and core-level spectra of several elements in the  $\text{Fe}_x\text{NbS}_2/\text{C}$  composite. For the XPS measurement, the sample surfaces were etched with Ar-ion sputtering for 300 s to remove surface contamination. The wide scan spectrum shown in Fig. 3a confirms the presence of Fe, Nb, S, and C elements in the synthesized composite. Fig. 3b shows the Fe 2p core-level spectra of the  $\text{Fe}_x\text{NbS}_2/\text{C}$  composite with the deconvoluted sub-profiles. The sub-profiles centered at 707.4 eV and 708.3 eV correspond to the  $2p_{3/2}$  orbital of  $\text{Fe}^{2+}$ , and the profiles at 709.8 eV, 711.1 eV, and 712.6 eV are attributed to  $\text{Fe}^{3+}$  [24,25]. The sub-profiles at 716.3 eV and 719.4 eV are related to the satellite peaks of  $\text{Fe}^{2+}$  and  $\text{Fe}^{3+}$ , respectively [24,25]. From these results, it is noted that the oxidation states of  $\text{Fe}^{3+}$  and  $\text{Fe}^{2+}$  are mixed in the composite. The Nb 3d core-level spectra with the deconvoluted results are shown in Fig. 3c. The peaks at 203.8 eV and 206.6 eV are assigned to the Nb  $3d_{5/2}$  and  $3d_{3/2}$  orbitals of the  $\text{Nb}^{(4-\delta)+}$  state, respectively [17,26]. The sub-profiles centered at 204.4 eV and 207.1 eV are attributed to  $\text{Nb}^{4+}$  and the peaks at 207.9 eV and 210.5 eV correspond to the  $3d_{5/2}$  and  $3d_{3/2}$  orbitals of  $\text{Nb}^{5+}$ , respectively [17,26]. Similar to the analysis results of Fe

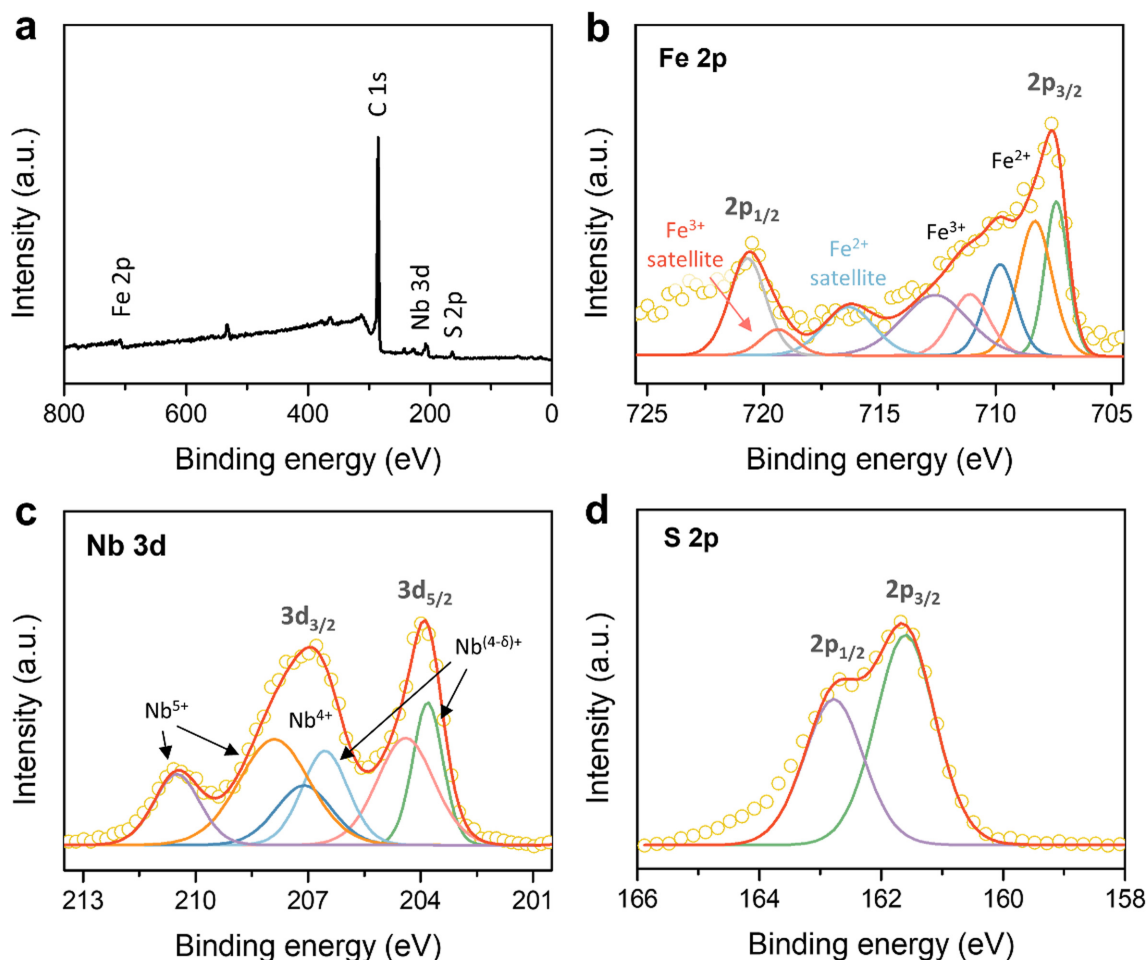


Fig. 3. XPS spectra of the  $\text{Fe}_x\text{NbS}_2/\text{C}$  composite: (a) wide scan spectrum and core-level spectra of (b) Fe 2p, (c) Nb 3d, and (d) S 2p

2p, different oxidation states of Nb exist in the composite. These results may be attributed to the fact that the two metals, Fe and Nb, co-exist in the disulfide material. Fig. 3d shows the S 2p core-level spectra with the deconvoluted profiles. The sub-profiles at 161.6 eV and 162.7 eV are related to the  $2p_{3/2}$  and  $2p_{1/2}$  orbitals of  $\text{S}^{2-}$ , respectively, which can be attributed to the metal-S bonds in the  $\text{Fe}_x\text{NbS}_2$  phase [20,21].

The morphology of the synthesized  $\text{Fe}_x\text{NbS}_2/\text{C}$  composite was characterized by electron microscopies with EDS elemental mapping. Fig. 4a and b show the FE-SEM and the corresponding EDS elemental mapping results of the  $\text{Fe}_x\text{NbS}_2/\text{C}$  composite. From the FE-SEM image, it was observed that the secondary  $\text{Fe}_x\text{NbS}_2$  particle measuring approximately a few micrometers consisted of very small primary particles. The EDS mapping results demonstrate that the Fe, Nb, S, and C elements were

uniformly distributed over the composite particle. Fig. 4c presents the low-magnification TEM image of the  $\text{Fe}_x\text{NbS}_2/\text{C}$  composite where the nano-sized  $\text{Fe}_x\text{NbS}_2$  primary particle is surrounded by amorphous carbon, which can be favorable for the enhancement of the electrochemical properties. The high-resolution TEM (HR-TEM) image and the fast Fourier transform (FFT, inset) pattern are shown in Fig. 4d. The lattice of  $\text{Fe}_x\text{NbS}_2$  was observed with a d-spacing of 2.89 Å, which could be attributed to the (010) reflection plane of  $\text{Fe}_x\text{NbS}_2$ . The inset FFT pattern also confirms the existence of the  $\text{Fe}_x\text{NbS}_2$  phase.

Fig. 5 presents the electrochemical test results of the  $\text{Fe}_x\text{NbS}_2/\text{C}$  composite electrode measured using the Li-ion half-cells. Fig. 5a shows the galvanostatic discharge/charge curves of the composite electrode for the first two cycles at a specific current of  $50 \text{ mA g}^{-1}$ . The first

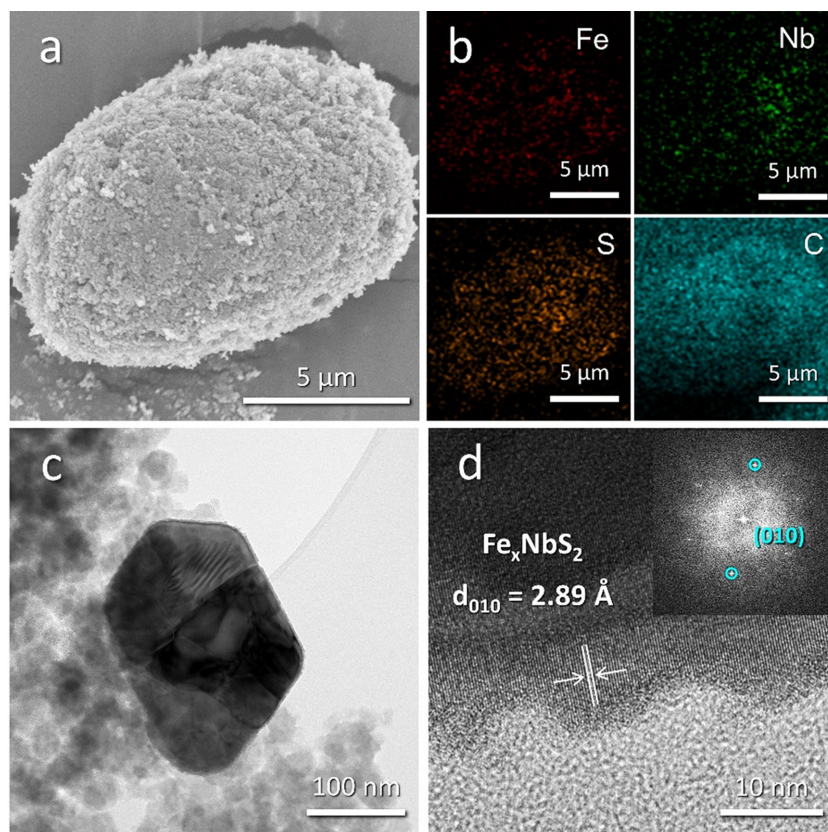


**Fig. 4.** (a) FE-SEM image, (b) EDS elemental mapping results, (c) low-magnification TEM image, and (d) HR-TEM image with FFT patterns (inset) of the  $\text{Fe}_x\text{NbS}_2/\text{C}$  composite

discharge and charge capacities are  $1007.3 \text{ mAh g}^{-1}$  and  $612.4 \text{ mAh g}^{-1}$ , respectively, with an initial coulombic efficiency of 60.8%. The reversible capacity is much higher than that of graphite electrodes. To examine the Li reaction mechanism of the composite electrode, Fig. 5b shows the differential capacity plots (DCPs) for the first two cycles. During the first Li insertion process (cathodic reaction), a broad peak at approximately 0.8 V vs.  $\text{Li}^+/\text{Li}$  can be observed, which corresponds to the sloping profile from 1.7 V to 0.2 V (vs.  $\text{Li}^+/\text{Li}$ ). As reported previously, the peak observed during Li insertion can be attributed to the conversion reaction of  $\text{Fe}_x\text{NbS}_2$  into Fe and Nb metals, and lithium sulfide (possibly  $\text{Li}_2\text{S}$ ) [17,18]. A peak at 1.3 V (vs.  $\text{Li}^+/\text{Li}$ ) can also be observed, appearing again at 1.4 V (vs.  $\text{Li}^+/\text{Li}$ ) during the second cycle. Because the reaction at the potential is reversible, these peaks could be attributed to the conversion reaction. Below 0.2 V (vs.  $\text{Li}^+/\text{Li}$ ), a sharp peak is observed, which becomes smaller in the second cycle. This indicates that the reaction in the potential range is partially irreversible, which may be

related to the formation of solid electrolyte interphase layers. Another possibility is that the conversion reaction is not fully reversible. During Li extraction (anodic reaction), the lithium sulfide and metals should be reversely transferred back to the transition metal sulfide and Li ions [17,18]. The existence of carbon in the composite may contribute to the Li insertion/extraction capacities.

Fig. 5c shows the cycling performance of the  $\text{Fe}_x\text{NbS}_2/\text{C}$  composite electrode measured at a specific current of  $50 \text{ mA g}^{-1}$ . After 50 cycles, a capacity of over  $420 \text{ mAh g}^{-1}$  was obtained with a capacity retention ratio of 69.2%. During the first few cycles, the reversible capacity decreases to a point and then remains constant afterward. This could be attributed to the microstructure of the composite where  $\text{Fe}_x\text{NbS}_2/\text{C}$  was well distributed in the carbon matrix. Therefore, the carbon matrix played an important role in buffering the volume change in  $\text{Fe}_x\text{NbS}_2$  during Li insertion/extraction cycles. Fig. 5d shows the rate performance of the  $\text{Fe}_x\text{NbS}_2/\text{C}$  composite electrode

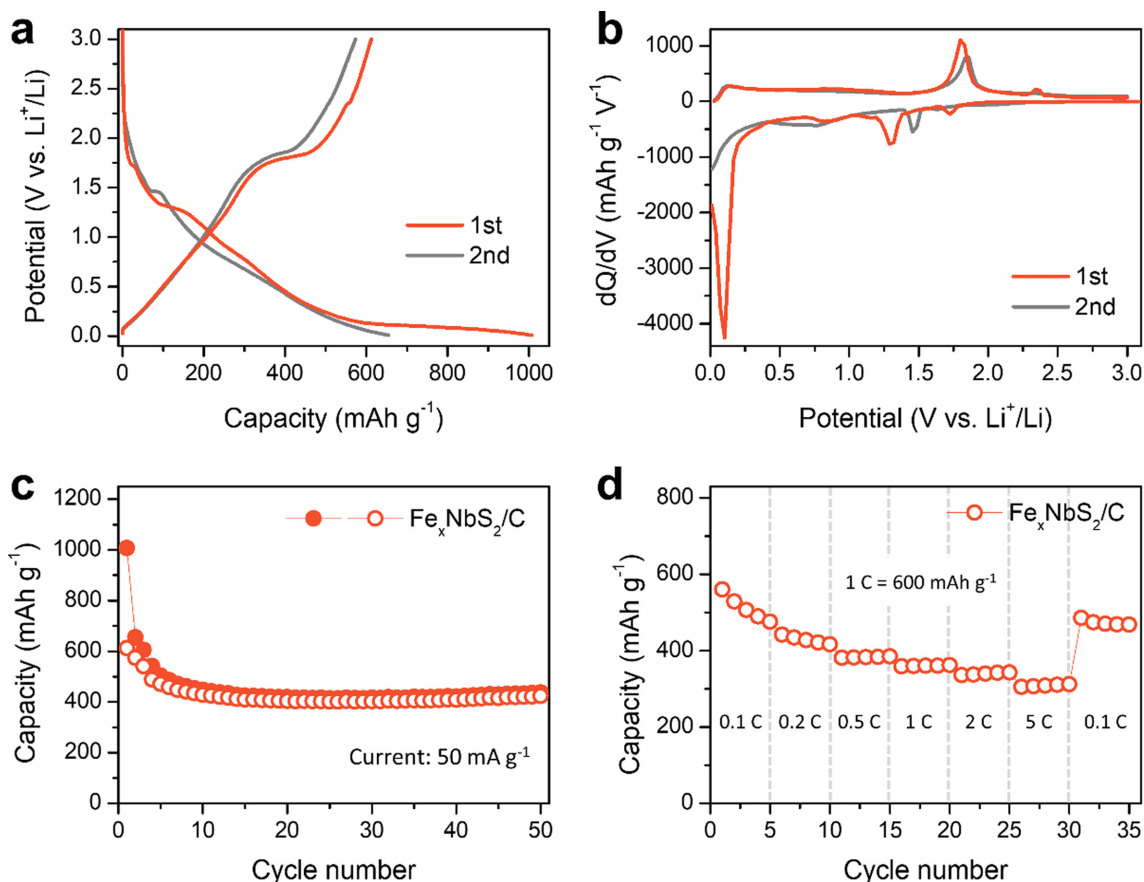


**Fig. 5.** Electrochemical test results of the  $\text{Fe}_x\text{NbS}_2/\text{C}$  composite anode: (a) galvanostatic discharge/charge curves for the initial two cycles at a specific current of  $50 \text{ mA g}^{-1}$ , (b) DCPs, (c) cycle performance at a specific current of  $50 \text{ mA g}^{-1}$ , and (d) rate performance at 0.1–5C

at rates between 0.1C and 5C. At a high rate of 5C, a capacity of approximately  $310 \text{ mAh g}^{-1}$  can be observed, which indicates that the composite electrode performed well at high-rate cycling. This can be attributed to two factors. First, the synthesized  $\text{Fe}_x\text{NbS}_2$  material has a lattice structure that facilitates the rapid transport of Li ions. Second, the incorporation of carbon promotes the rapid transport of electrons and ions through the electrode. From the results, it can be concluded that the TMD material and structural feature produced in the synthesis process of this study are suitable for obtaining good cycling stability and rate properties as electrode materials for Li-ion batteries.

#### 4. Conclusions

$\text{Fe}_x\text{NbS}_2/\text{C}$  composites were prepared by a facile HEMM method and heat treatment as an anode material

for Li-ion batteries. The crystal structure and chemical bonding states of the synthesized material were characterized by XRD and XPS analyses, respectively. The morphology with the elemental distribution was analyzed by FE-SEM and TEM measurements. The analysis results confirm that the composite was successfully prepared. The  $\text{Fe}_x\text{NbS}_2/\text{C}$  composite electrode was electrochemically tested in Li half cells. A reversible capacity of  $612.4 \text{ mAh g}^{-1}$  was obtained in the first cycle, which is much higher than that of graphite anodes. In addition, a capacity of approximately  $310 \text{ mAh g}^{-1}$  was observed at a high rate of 5C, demonstrating that the composite electrode is adequate for high-rate cycling. The performance can be attributed to the microstructure of the composite, which facilitates the rapid transport of Li ions. Therefore, it can be concluded that the TMD material with its structural features has great potential for applications in high-rate Li-ion battery electrodes.

## Acknowledgments

This work was supported by the Ministry of Education of the Republic of Korea and the National Research Foundation of Korea (NRF-2021S1A5A2A03065436).

## References

1. M. Winter, R. J. Brodd, What Are Batteries, Fuel Cells, and Supercapacitors?, *Chemical Reviews*, **104**, 4245 (2004). Doi: <https://doi.org/10.1021/cr020730k>
2. M. Li, J. Lu, Z. Chen, K. Amine, 30 Years of Lithium-Ion Batteries, *Advanced Materials*, **30**, 1800561 (2018). Doi: <https://doi.org/10.1002/adma.201800561>
3. F. Wu, J. Maier, Y. Yu, Guidelines and trends for next-generation rechargeable lithium and lithium-ion batteries, *Chemical Society Reviews*, **49**, 1569 (2020). Doi: <https://doi.org/10.1039/C7CS00863E>
4. H. Zhang, H. Zhao, M. A. Khan, W. Zou, J. Xu, L. Zhang, J. Zhang, Recent progress in advanced electrode materials, separators and electrolytes for lithium batteries, *Journal of Materials Chemistry A*, **6**, 20564 (2018). Doi: <https://doi.org/10.1039/C8TA05336G>
5. S. J. Hong, S. S. Kim, and S. Nam, Using Coffee-Derived Hard Carbon as a Cost-Effective and Eco-Friendly Anode Material for Li-Ion Batteries, *Corrosion Science and Technology*, **20**, 15 (2021). Doi: <https://doi.org/10.14773/CST.2021.20.1.15>
6. M. Winter, J. O. Besenhard, M. E. Spahr, P. Novák, Insertion Electrode Materials for Rechargeable Lithium Batteries, *Advanced Materials*, **10**, 725 (1998). Doi: [https://doi.org/10.1002/\(SICI\)1521-4095\(199807\)10:10<725::AID-ADMA725>3.0.CO;2-Z](https://doi.org/10.1002/(SICI)1521-4095(199807)10:10<725::AID-ADMA725>3.0.CO;2-Z)
7. H. Zhang, Y. Yang, D. Ren, L. Wang, X. He, Graphite as anode materials: Fundamental mechanism, recent progress and advances, *Energy Storage Materials*, **36**, 147 (2021). Doi: <https://doi.org/10.1016/j.ensm.2020.12.027>
8. K. Kim, H.-S. Kim, H. Seo, and J.-H. Kim, Electrochemical and Thermal Property Enhancement of Natural Graphite Electrodes via a Phosphorus and Nitrogen Incorporating Surface Treatment, *Corrosion Science and Technology*, **19**, 31 (2020). Doi: <https://doi.org/10.14773/CST.2020.19.1.31>
9. M. N. Obrovac, V. L. Chevrier, Alloy Negative Electrodes for Li-Ion Batteries, *Chemical Reviews*, **114**, 11444 (2014). Doi: <https://doi.org/10.1021/cr500207g>
10. C.-M. Park, J.-H. Kim, H. Kim, H.-J. Sohn, Li-alloy based anode materials for Li secondary batteries, *Chemical Society Reviews*, **39**, 3115 (2010). Doi: <https://doi.org/10.1039/B919877F>
11. H. Wang, S. Chen, C. Fu, Y. Ding, G. Liu, Y. Cao, Z. Chen, Recent Advances in Conversion-Type Electrode Materials for Post Lithium-Ion Batteries, *ACS Materials Letters*, **3**, 956 (2021). Doi: <https://doi.org/10.1021/acsmaterialslett.1c00043>
12. Y. Yang, H. Seo, J.-H. Kim, Electrochemical Characteristics of Synthesized Nb<sub>2</sub>O<sub>5</sub>-Li<sub>3</sub>VO<sub>4</sub> Composites as Li Storage Materials, *Corrosion Science and Technology*, **20**, 183 (2021). Doi: <https://doi.org/10.14773/cst.2021.20.4.183>
13. R. Sahoo, M. Singh, T. N. Rao, A Review on the Current Progress and Challenges of 2D Layered Transition Metal Dichalcogenides as Li/Na-ion Battery Anodes, *Chem. Electro. Chem.*, **8**, 2358 (2021). Doi: <https://doi.org/10.1002/celec.202100197>
14. T. Zhao, H. Shu, Z. Shen, H. Hu, J. Wang, X. Chen, Electrochemical Lithiation Mechanism of Two-Dimensional Transition-Metal Dichalcogenide Anode Materials: Intercalation versus Conversion Reactions, *The Journal of Physical Chemistry C*, **123**, 2139 (2019). Doi: <https://doi.org/10.1021/acs.jpcc.8b11503>
15. X. Zhang, Z. Lai, Q. Ma, H. Zhang, Novel structured transition metal dichalcogenide nanosheets, *Chemical Society Reviews*, **47**, 3301 (2018). Doi: <https://doi.org/10.1039/C8CS00094H>
16. Q. Yun, L. Li, Z. Hu, Q. Lu, B. Chen, H. Zhang, Layered Transition Metal Dichalcogenide-Based Nanomaterials for Electrochemical Energy Storage, *Advanced Materials*, **32**, 1903826 (2020). Doi: <https://doi.org/10.1002/adma.201903826>
17. J. Zhang, C. Du, Z. Dai, W. Chen, Y. Zheng, B. Li, Y. Zong, X. Wang, J. Zhu, Q. Yan, NbS<sub>2</sub> Nanosheets with M/Se (M = Fe, Co, Ni) Codopants for Li<sup>+</sup> and Na<sup>+</sup> Storage, *ACS Nano*, **11**, 10599 (2017). Doi: <https://doi.org/10.1021/acsnano.7b06133>
18. C. Pan, J. Kang, Q. Xie, Q. Li, W. Yang, H. Zou, S. Chen, T-Nb<sub>2</sub>O<sub>5</sub>@NbS<sub>2</sub>@C Composites Based on the Intercalation–Conversion Mechanism as an Anode Material for Li-Ion Batteries, *ACS Applied Energy Materials*, **4**, 12365 (2021). Doi: <https://doi.org/10.1021/acsaem.1c02165>
19. Y. Liao, K.-S. Park, P. Singh, W. Li, J. B. Goodenough, Reinvestigation of the electrochemical lithium intercalation in 2H- and 3R-NbS<sub>2</sub>, *Journal of Power Sources*, **245**, 27 (2014). Doi: <https://doi.org/10.1016/j.jpowsour.2013.06.048>
20. D. Gopalakrishnan, A. Lee, N. K. Thangavel, L. M.

- Reddy Arava, Facile synthesis of electrocatalytically active  $NbS_2$  nanoflakes for an enhanced hydrogen evolution reaction (HER), *Sustainable Energy & Fuels*, **2**, 96 (2018). Doi: <https://doi.org/10.1039/C7SE00376E>
21. X. Ou, X. Xiong, F. Zheng, C. Yang, Z. Lin, R. Hu, C. Jin, Y. Chen, M. Liu, In situ X-ray diffraction characterization of  $NbS_2$  nanosheets as the anode material for sodium ion batteries, *Journal of Power Sources*, **325**, 410 (2016). Doi: <https://doi.org/10.1016/j.jpowsour.2016.06.055>
22. Q. Hao, D. Wang, B. Zhu, S. Zeng, Z. Gao, Y. Wang, B. Li, Y. Wang, Z. Tang, K. Tang, Facile synthesis, structure and physical properties of  $3R-A_xNbS_2$  ( $A = Li, Na$ ), *Journal of Alloys and Compounds*, **663**, 225 (2016). Doi: <https://doi.org/10.1016/j.jallcom.2015.12.094>
23. L. Ehm, S. Vogel, K. Knorr, P. Schmid-Beurmann, W. Depmeier, X-ray powder diffraction and  $^{57}Fe$  Mössbauer spectroscopy study on  $Fe_{0.47}NbS_2$ , *Journal of Alloys and Compounds*, **339**, 30 (2002). Doi: [https://doi.org/10.1016/S0925-8388\(01\)01980-6](https://doi.org/10.1016/S0925-8388(01)01980-6)
24. Z. Wang, C. Liu, G. Shi, G. Wang, H. Zhang, Q. Zhang, X. Jiang, X. Li, F. Luo, Y. Hu, K. Yi, Preparation and electrochemical properties of electrospun  $FeS$ /carbon nanofiber composites, *Ionics*, **26**, 3051 (2020). Doi: <https://doi.org/10.1007/s11581-020-03455-2>
25. J. E. Thomas, W. M. Skinner, R. S. t. C. Smart, A comparison of the dissolution behavior of troilite with other iron(II) sulfides; implications of structure, *Geochimica et Cosmochimica Acta*, **67**, 831 (2003). Doi: [https://doi.org/10.1016/S0016-7037\(02\)01146-8](https://doi.org/10.1016/S0016-7037(02)01146-8)
26. K. Izawa, S. Ida, U. Unal, T. Yamaguchi, J.-H. Kang, J.-H. Choy, Y. Matsumoto, A new approach for the synthesis of layered niobium sulfide and restacking route of  $NbS_2$  nanosheet, *Journal of Solid State Chemistry*, **181**, 319 (2008). Doi: <https://doi.org/10.1016/j.jssc.2007.12.002>